(Abstract No 208)

Extension of SPIS to simulate dust electrostatic charging, transport and contamination of lunar probes

P. Sarrailh, S.L.G. Hess, J.-C. Matéo-Vélez, F. Cipriani, D. Rodgers, A. Hilgers, B. Jeanty-Ruard,

B. Thiébault, J. Forest, F. Honary, S.R. Marple

***Abstract*— A modification of the Spacecraft Plasma Interaction Software has been undertaken under ESA contract 4000107327/12/NL/AK (SPIS-DUST). The primary goal is to provide mission designers with an engineering tool capable of predicting charged dust behavior in a given plasma environment involving a spacecraft / exploration unit in contact with complex topological features at various locations of the Moon's surface. The tool also aims at facilitating dust contamination diagnostics for sensitive surfaces such as sensors optics, solar panels, thermal interfaces, etc.**

In this paper, the new user interface and the new numerical solvers developed in the frame of this project are presented. The pre-processing includes the building of a 3D lunar surface from a topological description (i.e. a point list), an interface to position the spacecraft and a merging interface for the spacecraft elements in contact with the lunar surface. Concerning the physical models, the new solvers have been developed in order to model the physics of the ejection of the dust from the soils, the dusts charging and transport in volume and the dust interaction and contamination of the spacecraft. The post-processing includes the standard outputs of SPIS for the electrostatic computation and the plasma plus dedicated instruments for the diagnosis of the dusts. Test cases are presented in order to demonstrate the new capabilities of this version of SPIS.

Keywords—component; formatting; style; styling; insert (*key words****)***

I. INTRODUCTION

Following the Apollo missions, it has been discovered that the lunar dusts are potential threats to any mission on or close to the moon surface. These sub-micron sized dusts are highly abrasive, so that friction with surfaces can wear down materials and reduce material lifetimes, and they are highly sticking due to their small size and their electrostatic charge. They are also potential health hazard for astronauts.

These particles have been observed to "levitate" above the lunar surface and to form a haze that may extend to several tens of kilometers in altitude. The dust motion is though to be due to the conjugation of dust ejection by micro-meteorite impacts and by electrostatic forces. The latter is expected to be amplified by the lighting variation on the irregular moon surface, in particular close to the crater rims. The ejected dust can be deposited on landers on the moon surface.

To investigate for potential lunar mission risks, SPIS capacities were extended to include the modeling of the lunar dust charging, ejection, dynamics in the plasma and deposition in the frame of an ESA contract (SPIS-DUST).

The present paper details the extension to both the User Interface, which now permits one to build a simulation geometry based on Lunar topological data and to include a lander in it, and on the numerical core, which was developed to handle the physics of dust charging and a better description of the plasma sheath above the ground. The user interface and the numerical core also have been extended to allow for the use of new diagnosis instruments related to the dust motion and characteristics in and out of the simulation domain.

The major developments are presented in sections II and III (first concerning the user interface and then concerning the numerical core). Then, the forth section presents the outputs of a 3D test case and displays in particular the outputs of some of the new instruments.

II. THE USER INTERFACE

A. Geometry definition

In order to ease studies targeting a precise site on the moon, SPIS now offers the possibility to generate the simulation domain directly from a set of « geographical» 3D coordinates of the lunar surface. This is performed in five steps (Figure 1).

First, the list of coordinates is loaded in SPIS.

Second, the boundary of the 2D surface is automatically computed by SPIS. The border identification is based on the Gift Wrapping Algorithm. It starts with the point in the list with the minimal abscissa and then iteratively searches for the neighboring point on the border. This point is found by selecting pairs of points which form a triangle with the last known point of the border: if the triangle is clockwise, the second point of the triangle is retained, otherwise the third is. The point retained whatever the third triangle summit is the next neighboring point of the border. The performances of the

(Abstract No 208)

implemented algorithms are fully acceptable for the targeted configurations. For very large systems, it remains possible to compute a rectangular border as an alternative.

Third, the surface is meshed as a planar surface using Gmsh as the mesher.

Then, the elevation of the surface is computed in an operation called kriging [1][2][3]. The first step of the kriging is the selection of the neighboring points of the node x_0 for which one the altitude has to be computed. The space around the node is divided in four quadrants, the size of which is defined by the user and in which a given maximum number of neighbors will be searched for. If no neighbor is found, the node x_0 is removed from the mesh. A covariance matrix **K** is computed where each value (i,j) correspond to a covariance factor function of the distance between the neighbor points x_i and x_j. A covariance vector $\mathbf{K_0}$ is computed, where the component i correspond to a covariance factor function of the distance between the points x_i and x_0. An altitude vector **Z** is defined with as components the corresponding elevations of the neighboring points. The final kriging interpolation of the altitude z_0^* of the point x_0 is given by: $z_0^* = Z^t K^{-1} K_0$.

Finally, the computational volume is defined by extrusion of the surface border.

The ground tessellation is able to generate a mesh with 600 elements from about 10^5 ground coordinates in about 15 seconds on a standard desktop PC. However, some parts of the algorithm are non-linear so that large systems may be considered with care.

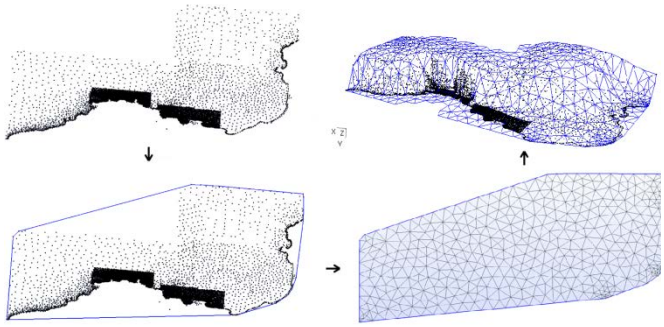

Figure 1: Definition of the lunar surface mesh from a list of ground coordinates.

B. Lander insertion

If a lander is to be inserted in the simulation, it is needed to apply a careful processing of the interface between the lander mesh and the surface mesh.

To do so, an algorithm was implemented in SPIS which detects the N closest pairs of lunar and spacecraft surfaces (N being set by the user). The distance between the surfaces is that of their barycenter. Between these N pairs, the user chooses those which will be merged. New faces are then created that links the lander to the ground. If needed, the geometry of the ground can be locally changed, not that of the lander.

C. Definition of the material properties

SPIS predefined materials did not include any material approaching that of the lunar surface. In order to simulate the environment of a probe on the lunar surface, we defined two lunar materials which only differ by their conductivity. The conductivity of lunar dust varies a lot between the samples returned back from Apollo missions. From [4] p 531, the bulk conductivity of Apollo 15 soil (15301,38) and Apollo 16 rock (65015,6) depend on the temperature. In addition, [4] reports that UV illumination increases the conductivity of soils by a factor 10^6, comparable to that produced by a temperature of 800°C. As a result, we defined a resistive lunar surface material with a bulk conductivity of = 10^{-18} $\Omega^{-1}.m^{-1}$ and a surface resistivity of = 10^{18} Ω, and a conductive one.

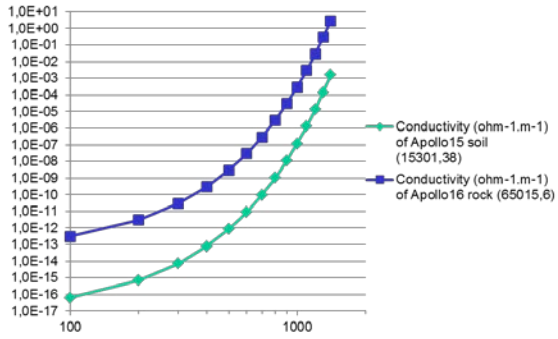

Figure 2: Bulk conductivities ($ohm^{-1}.m^{-1}$) of two lunar samples as a function of the temperature (K), from [4].

The main property of this material is the distribution of the dust sizes. The dust size distribution is taken from [4], p306, referred as 71501,1 Mare and presented on Figure 3. The initial plot did not clearly present particles of radii lower than 1 µm. As a result, we extrapolated the radius distribution function with a fit $f(r) = Ar^2 \exp(-Br^2)$.

The lunar material current density at normal sunlight incidence angle is 4,5 $\mu A/m^2$ at 1 AU for lunar dust [5]. Concerning the secondary emission from particle impact [5], it is assumed to be low at the surface, but once the dusts are emitted in the volume, the secondary emission model of Chow et al.,1993 [6] is implemented for the emission induced by electron impact. This model depends on three parameters: the inverse of the energy required to excite a single secondary electron ($K = 0.01 eV^{-1}$), the inverse of the absorption length for secondary electrons ($\alpha = 10^8 m^{-1}$), and the Whiddington constant for the rate loss with distance ($a = 10^{14} V^2.m^{-1}$).

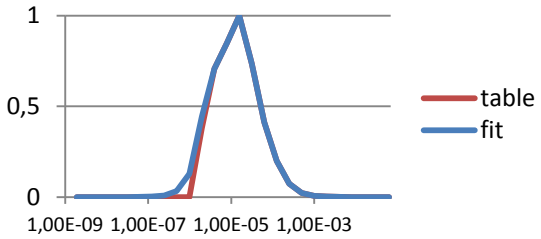

Figure 3 : Distribution of the dust radii (m) from the table given in [4] and the fit in used in SPIS.

(Abstract No 208)

D. SPIS Instruments

New data field probes / output modules called 'instruments' were developed to diagnose the dust emission, dynamics and deposition:

A dust detector uses particle backtracking to accurately determine the dust deposition over the surfaces.

A dust trajectory sensor permits one to follow the trajectory of test particle dusts. The trajectories are displayed in the SPIS user interface. The charge and velocity of the test particles are monitored along their trajectory.

A dust distribution sensor permits one to monitor the dusts inside a spherical volume. The dust individual properties, their distributions and their mean values are computed a can be displayed. A table of all the dusts and their properties can be saved as ASCII or binary NetCDF files. An example of such a distribution is shown on Figure 7.

Finally, an instrument has been developed which computes the density of dusts in a volume of space located above a given altitude (open boundary) where the charge of dust consistently varies by interacting with the local plasma.. The dusts reaching the open boundary of the simulation get their charge fixed and their trajectory is then computed as:

$$\frac{d^2z}{dt^2} = \frac{v_\theta^2 - gR}{z+R} + \frac{q_d}{m_d} E_z e^{-z/\lambda_D} \qquad (1)$$

From these trajectories the density of dust as a function of altitude and of the dust radii is computed. An example of this instrument output is shown on Figure 8.

III. Physical Modeling

A. Plasma sheath

Because it is not intended to simulate the Moon or any other celestial body entirely, the SPIS simulation domains are quasi-1D boxes, with an open face through which the solar wind plasma is injected, a celestial body surface face both absorbing the plasma and emitting photo- and secondary electrons as well as dust, and four boundary faces either reflecting or periodic. In this configuration, the quasi-neutrality of the plasma at the open boundary (which figures undisturbed solar wind) is not self-consistently ensured: depending on the electric potential profile across the domain, solar wind species could either be totally absorbed by the surface or be totally reflected by the electric field. The density at the open boundary in the second case would be twice that in the first case. Moreover, some of the photo-electrons emitted from the surface may also reach the open-boundary and participate to the non-neutrality of the plasma. Thus, it is needed to adjust the influx of solar wind electrons to ensure quasi-neutrality at the open boundary. In SPIS, this adjustment is performed automatically.

The computation is based on the motion of the different populations along a potential profile such as that found by [7] (Panel b of Figure 4): solar wind electron (e^-_{sw}), solar wind ions H+ and photoelectrons (e^-_p). The H^+ density at the open boundary is the easiest to obtain: Since the H^+ bulk velocity is larger than their thermal velocity and large enough to overcome the electric potential effects, the H^+ density is constant in the domain and corresponds to the integral of the H^+ distribution function.

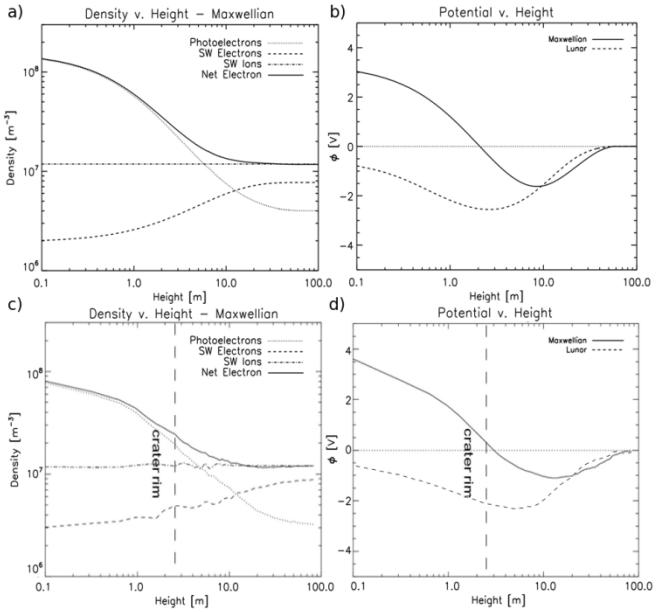

Figure 4: Density (a,c) and potential (b,d) profiles for the simulation of [7] and the test case, respectively.

In SPIS, the photo-electron injection is parameterized by the surface material current density at normal sunlight incidence angle and by some parameters proper to the photo-electron distribution (such as the temperature for a Maxwellian distribution, but also optionally by higher order moments). The density of photo-electrons at the open boundary is determined by computing the current of photo-electron at the peak of the potential barrier (or just above the surface if it is more negative) and by dividing it by the mean velocity of the photo-electrons at the open boundary. For a Maxwellian distribution this velocity is

$$v_{p\infty} = \sqrt{\frac{\frac{2}{\pi} k T_{p+e\Delta V_{dip}}}{m_{e/2}}}. \qquad (2)$$

ΔV_{dip} is the minimum potential in the simulation minus the potential at the open boundary, assuming that it is quasi-1D. In order to avoid to use a local surface potential as the averaged minimum potential in the plasma, ΔV_{dip} is computed by either taking the minimum of the potential above the surface plus a fraction of the Debye length (amplitude of the potential barrier) or the averaged potential on the surface, depending on which is the smallest (ΔV_{dip} is always positive or zero).

For a planar and conductive surface, lighted up by the sun at zenith, the current at the peak of the potential barrier is the current at the surface J_p multiplied by a factor depending on the potential difference between the surface and the potential barrier and on the photo-electron distribution function. This factor is

$$a = exp\left(\frac{-\max\left(0, e\left(V_{surf} - V_{dip}\right)\right)}{kT_p}\right) \qquad (3)$$

for a Maxwellian photo-electron distribution, with V_{surf} the potential of a surface element.

(Abstract No 208)

The photo-electron current emitted by the surface depends in the lighting, so that a multiplicative term

$$b = (\vec{\varphi}.\vec{n}) \quad (4)$$

must be applied for non-zenithal lighting (with $\vec{\varphi}$ the sun direction and $\vec{n}$ the normal to the surface element).

For non-planar surface, the shadowing of the surface elements must be computed (in which case the nominal flux, J_p, is proportional to the lighted surface). Also in this case, a multiplicative term must be applied, that takes into account the direction of emission of the electron, $\vec{n}$, relative to the normal to the average plane of the surface, $\langle\vec{n}\rangle$, along which the total current is computed. For an isotropic distribution, this term is

$$c = 1 - \pi^{-1} acos(\vec{n}.\langle\vec{n}\rangle). \quad (5)$$

Finally, for dielectric surface, another multiplicative term must be added to account for the recollection of electron emitted on surfaces with a potential lower than the average surface potential. It can be modeled as a misalignment of the direction of emission due to an electric field parallel to the surface. Based on kinetic consideration and for a Maxwellian distribution this term is

$$d = 1 - \pi^{-1}\mathrm{atan}\left(-\frac{max\left(0,e\left(\langle V_{surf}\rangle - V_{surf}\right)\right)}{kT_p}\right), \quad (6)$$

where $\langle V_{surf}\rangle$ is the average surface potential.

Thus, the density of photo-electrons at the open boundary is total current through the potential barrier, obtained by the sum of the currents emitted by each surface elements multiplied by the above terms and by the element surface, S_i, divided by the electrons charge, velocity at the open boundary and by the potential barrier cross section, A.

$$n_{p\infty} = \frac{\sum_{i\in surface} J_{pi} a_i b_i c_i d_i S_i}{-e v_{p\infty} A}. \quad (7)$$

The solar wind electron distribution is a bit more difficult to compute than the ion one, because their thermal velocity is larger than their bulk velocity and their kinetic energy of the same order than the potential energy. Assuming a Maxwellian distribution, the e^-_{sw} density at the top boundary is

$$n_i - n_{p\infty} = \frac{n_{e0}}{2}\left(1 + 2\,\mathrm{erf}\left(\frac{v_d}{v_{Te}}\right) - \mathrm{erf}\left(\frac{v_d}{v_{Te}} - \sqrt{\frac{e\Delta V_{dip}}{kT_e}}\right)\right). \quad (8)$$

n_{e0} is the amplitude of the e^-_{sw} distribution we want to compute, v_d is the bulk velocity of the solar wind and the thermal velocity is $v_{Te} = \sqrt{(2kT_e)/m_e}$. SPIS solves the above equation and determine the influx ($\propto n_{e0}$) for any isotropic distribution. Panel c and d of Figure 4 shows the density and electric potential profiles for the test case, respectively.

B. Dust emission

1) Dust distribution at the surface

The distribution function of the dust on the Lunar surface is controlled by the material properties defined on the Local Parameter editor. In the dust version of SPIS, the dust emission from the surface is automatically created if a surface material displays dust material properties (at least the definition of a radius distribution function).

The first step of the interaction computation is the conversion of the distribution function of dust in radius, mass and shape from a continuous function into a discrete distribution function on the lunar/asteroid surface. Then, the distribution function is converted into a macroparticle list sampling the particles on the surface.

The particle distribution function is randomly sampled in a equiprobable way, meaning that all the macroparticles have the same statistical weight and thus represent the same number of physical dusts. However, this choice is not optimal in most of the cases as the size of the dusts that are able to fly is not that of the most numerous ones on the surface. Thus, it is more efficient to sample more small dust macroparticles (with radius less than 1µm) than larger ones that stick on the lunar surface due to the gravity. A global parameter of SPIS permits one to control the weighting of the macroparticle sampling probability.

The dust surface density (number of dust per square centimeters) can be defined by the user. Otherwise, the code computes a density considering that the distribution function on the surface is the same as in volume (provided by data from the literature) and that the surface density corresponds to:

$$n_s = \frac{\sum_{i=0}^{N} w_i}{\sum_{i=0}^{N} \pi r^2 w_i}, \quad (9)$$

where w_i is the statistical weight of the i^{th} macroparticle and N is the number of macroparticles at the surface. In this case, the effective charged surface area greater than the geometrical surface area.

2) Dust charging on the surface

The global charge of a surface element is computed from the Gauss law, given the electric field on the surface. It permits to have a total charge consistent with the sheath.

$$Q_S = \varepsilon_0 E_S S \quad (10)$$

S being an element of the surface, Q_S and E_S are the charge and electric field on this surface, respectively.

Between two iterations (time step), the variation of the surface charge, ΔQ_S, is computed and the charge difference is distributed between all the dusts on the surface depending on their radius and ensuring that the total charge is conserved. A linear dependence of the charge of the dust with the radius is chosen as the potential of the dust on the surface is considered to be the potential of the surface and the capacitance in spherical symmetry is:

$$\mathrm{C} = 4\pi\varepsilon_0 \mathrm{r_d} \quad (11)$$

As the dusts on surface are not perfect sphere, the relation transforms into:

$$\mathrm{Q_D} = \mathrm{CV} \sim \mathrm{r_D V} \quad (12)$$

Thus, the charge variation on the surface is distributed between the macroparticles such as

$$\Delta Q_D \sim r_D \times \Delta Q_S \quad (13)$$

and

$$\sum_N w\,\Delta Q_D = \Delta Q_S \quad (14)$$

(Abstract No 208)

It permits to get a consistent charge evolution between each step. Finally, a field enhancement factor β due to microscopic structures is introduced, that accounts for the inhomogeneity of the charging at the surface, mainly due to its microscopic roughness. It is modeled as regions of enhanced electric field (by a factor β) that cover a fraction β^{-1} the surface. At the scale of the dust macroparticles, it is translated into increasing the charge of the dust by a factor β and decreasing the statistical weight by the same factor.

$$\Delta Q_D \rightarrow \beta\, \Delta Q_D \; and \; w \rightarrow \frac{w}{\beta} \tag{15}$$

This can be understood as introducing a differential charging in the physical dusts represented by a single macroparticle: a fraction β^{-1} of these physical particles gets all the charge deposited on all the physical dusts.

3) Force balance on the surface dusts

SPIS takes into accounts several forces that applies to the dusts on the surface: gravity and electrostatic forces at large scale (E_S, with a microscopic enhancement β factor) and at smaller scales (cohesive forces). It can also accounts for seismic forces (defined by their amplitude and frequency).

The electrostatic force is computed from the projection of the electric field on the barycenter of the surface elements, the charge of the dusts and the field amplification factor due to local amplification structures.

$$\overrightarrow{F_E} = Q_D \beta \left(\vec{E}.\vec{n}\right)\vec{n} \tag{16}$$

The amplification factor of the electric field has thus a huge influence on the electrostatic force as it appears in the electric field and in the dust charge (quadratic influence).

The gravity force is directly the product of the gravity vector projection on surface element and the mass of the dust.

$$\overrightarrow{F_G} = m_D(\vec{g}.\vec{n})\vec{n} \tag{17}$$

The gravity force is zero where the surfaces are orthogonal to the gravity vector, causing some problems in comparison to the reality where the roughness of the surface prevents the gravity to be completely orthogonal to the local surface.

The Van der Waals force is modelled as

$$\overrightarrow{F_C} = -KS^2.r_D\vec{n}. \tag{18}$$

From the literature, the factor K is about 5e-2 kg/s^2 and *S* is about 0.8 [8][9]. According to [10], it seems impossible to launch particles submitted to such a force (1 µm size dusts undergo a 10^{-8} N force). As a result, the authors suggested that the dust cleanliness and the non-uniform charge could lead to a strong decrease of the cohesion force and to a strong increase of the electrostatic force, respectively. In the present model, we consider that KS^2 is equal to 10^{-6} kg/s^2.

When the sum of force is positive, the dust is ejected from the surface.

C. Dust dynamics

Once ejected, the dust dynamics is computed in a way similar to any other particle, the seismic forces do not apply anymore, but the magnetic field does. The electrostatic force is computed without the enhancement factor anymore, as it results from local microscopic inhomogeneities in the field at the surface. However, the particle is emitted with its enhanced charge (but with a weight divided in consequence).

Nevertheless, the dust dynamics differ from that of the other particles on the fact that its charge varies with time, both because of plasma collection on the dust and of secondary emission.

SPIS offers several ways of computing the dust charging due to plasma collection, whether based on OML or Monte Carlo schemes. In any case, the dust potential is computed considering a capacitive coupling:

$$\phi_d(t) = \frac{Q_d(t)}{C} = \frac{Q_d(t)}{4\pi\varepsilon_0 r_d(1+r_d/\lambda_D)} \tag{19}$$

From this potential, the collected current, J_c, is either computed from the OML model (mandatory for fluid populations) and/or by a Monte Carlo scheme for PIC populations.

The secondary electron emission under electron impact is also computed (that from proton impact is neglected after [5]). The model of Chow et al.,1993 [6] is implemented. The material parameters of this model are defined as local parameters in SPIS. The electron yield depends on the primary electron energy and the dust radius. Solving Chow et al., 1993 equation being computationally demanding, the model solutions are tabulated against energy and dust radius at the beginning of the simulation and later interpolated. The dust potential affects the secondary emission both by determining the primary electron collection, but also by acting on their energy. The net secondary electron emission (SEEE) current, J_s, is scaled by the potential difference between the dust and the plasma.

The total charge of the dust is updated at each time step following the current balance:

$$\frac{dQ_d}{dt} = J_c + J_s + J_p \tag{20}$$

where J_p is the photo-emission current. The current density at normal sunlight incidence angle is 4,5 µA/m^2 at 1 AU for lunar dust [5]. On the surface, the flux is moderated by the sun incidence angle (see section III.A). For dust in the plasma, the photocurrent is either maximal when irradiated or zero when shaded by an element of surface. The dust photoelectron current is the multiplication of the photoelectron current density by the dust cross section.

On the lunar surface, the energy distribution function of photoelectron is Maxwellian by default, with a temperature of 2.2 eV, but the distribution determined by Feuerbacher et al., 1972 [12] can also be used by the mean of global parameters defining the high order moments of the photoelectron distribution:

$$f_p(v) = \frac{n_p}{\pi\Gamma\left(\frac{7}{4}\right)v_p^7} v^4 exp\left[-\left(\frac{v}{v_p}\right)^4\right] \tag{21}$$

The relation is normalized following the photoemission current provided in the standard material properties. For dusts in the plasma the by Feuerbacher-1972 distribution is always

(Abstract No 208)

used. As for the SEEE, the net current emitted depends on the potential difference between the dust and the plasma, ΔV. For a Maxwellian distribution the photoelectron current from the dust in the plasma (recollection being accounted for) is :

$$I_p = J_p \pi r^2 exp\left(-\frac{\max(0, e\Delta V)}{kT_p}\right). \quad (22)$$

It is also used as an approximation to estimate the photo-electro current from the dust for the Feuerbacher distribution.

IV. Test Case

Several test cases were run during the SPIS-DUST development and validation simulations are currently performed. In the present paper, we limit ourselves to a single 3D case which simulates the sheath and the dust dynamics above a crater. The simulation domain is half a cylinder, with the lunar surface and the open boundary being the two cylinder ends. The other half of the cylinder is not simulated because it is the image of the simulated domain by symmetry. The cylinder radius is 10 meter. The crater is has a radius of 5 meter and a depth of 2 meters and is surrounded by a 0.5 meter wide rim. The boundary conditions on the other domain surfaces are reflective.

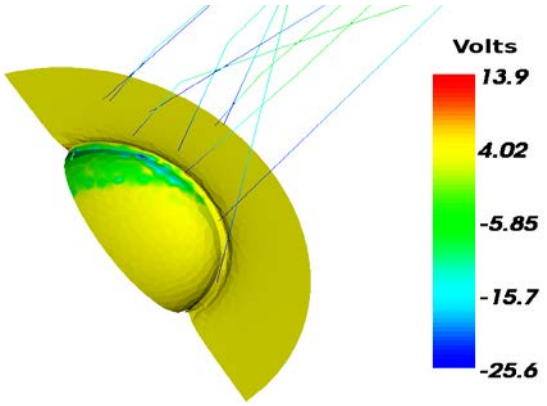

Figure 5: Surface potential and test-particle dust trajectories

The lunar surface outside the crater is conductive, as no obstacle may bring shade on it, whereas the surface the crater is dielectric (we do not precisely separate shaded and lighted surfaces in this simulation). As the sunlight incidence angle is 45° in the simulation, the surface of the crater charge differentially.

In spite of the inclination of the sun direction, the direction of arrival of the solar wind is normal to the surface because of the reflective boundary conditions. The solar wind density is 12 cm^{-3} (exact for ion, automatically scaled by SPIS for the electrons), with equal temperatures of 10 eV for ions and electrons. Both populations have a bulk velocity of 400km/s.

The simulation runs until it reaches a stationary state.

The simulation is run twice with different photo-electron distributions, once with a 2.2 eV Maxwellian distribution, and once with a Feuerbacher distribution. The plasma species densities for the Maxwellian case and the potential profiles for both cases are shown on Panels c and d of *Figure 4* and compared with results of [7] (Panels a and b of the same Figure). Although the parameters between our and simulations are slightly different (1D vs 3D, solar inclination ...) the profiles are similar. The profile is computed along a line passing through the crater center, and the altitude of the crater rim, is indicated.

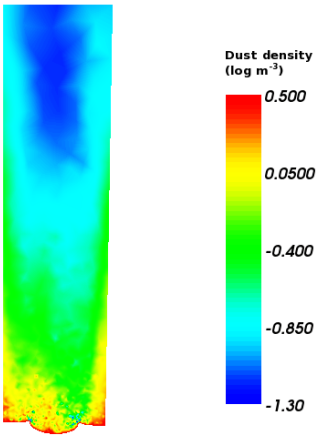

Figure 6 : Dust density on a simulation domain cut

Figure 5 shows the surface potential and some dust trajectories and Figure 6 shows a cut of the dust density in the simulation domain. The dust density is lower in and above the crater, although it is the preferential region of dust emission. This is actually due to the larger velocities of the dusts in these regions.

Figure 7 shows the dust radius distributions in the crater and close to the open boundary. These distributions are computed by a new SPIS instrument, which also computes the charge and mass distributions. The distributions show that dust grains larger than a micron do not reach altitudes larger than a few meters.

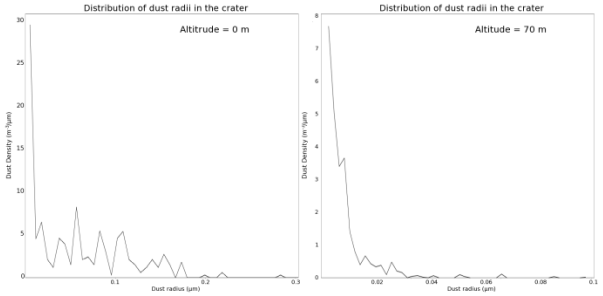

Figure 7: Dust size distributions along the crater center line inside the crater and close to the open boundary.

Figure 8 shows the density of dusts as a function of their altitude and radius above the simulation box. This distribution is computed by a new SPIS instrument which computes the trajectories of the dusts crossing the open boundary, assuming that their charge does not evolve out of the simulation domain. Nanometer dusts can reach several tens of kilometers, whereas dusts larger than 0.1 microns do not cross the open boundary (80 m of altitude).

(Abstract No 208)

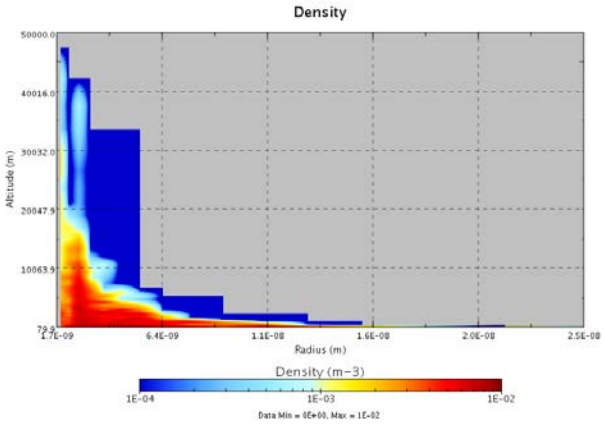

Figure 8 : Density of dust above the simulation domain, as a function of altitude and dust radius.

ACKNOWLEDGMENT

The present study and the modifications to the Spacecraft Plasma Interaction Software have been undertaken under ESA contract 4000107327/12/NL/AK (SPIS-DUST).

REFERENCES

[1] Bailly du Bois P., Automatic calculation of bathymetry for coastal hydrodynamic models, Computers and Geosciences, doi:10.1016/j.cageo.2010.11.018 , 2011

[2] Ricardo A. Olea, Geostatistics for engineers and earth scientists, Norwell, Massachussetts 02061 USA, 303p, 2003

[3] B.Jeanty-Ruard, B.Thiebault, Documentation sur l'évolution des algorithmes d'interpolation, Ifremer BMGTools Project, internal technical documentation, contract ref. 12/2.212.883, 2012

[4] Heiken, G., Vaniman, D., & French, B. M. (Eds.). "Lunar sourcebook: A user's guide to the Moon", Cambridge University Press, 1991.

[5] Willis, R. F.; Anderegg, M.; Feuerbacher, B.; Fitton, B., "Photoemission and Secondary Electron Emission from Lunar Surface Material", Proceedings of the 6th ESLAB Symposium, Noordwijk, September 26-29, 1972, edited by R.J.L. Grard. Astrophysics and Space Science Library, Vol. 37, p.389, 1973

[6] Chow, V. W., D. A. Mendis, and M. Rosenberg, "Role of grain size and particle velocity distribution in secondary electron emission in space plasmas", J. Geophys. Res., 98(A11), 19065–19076, 1993.

[7] Poppe, A., and M. Horányi, "Simulations of the photoelectron sheath and dust levitation on the lunar surface", J. Geophys. Res., 115, A08106, Aug. 2010.

[8] Perko, H., Nelson, J., and Sadeh, W. (2001). "Surface Cleanliness Effect on Lunar Soil Shear Strength." J. Geotech. Geoenviron. Eng., 127(4), 371–383.

[9] A. R. Dove, "Experimental investigations of the lunar photoelectron environment and related dust dynamics," University of Colorado, USA, 2012..

[10] Hartzell, C. M., and D. J. Scheeres (2013), "Dynamics of levitating dust particles near asteroids and the Moon", J. Geophys. Res. Planets, 118, 116–125, jan. 2013

[11] Saito, Y., et al., Solar wind proton reflection at the lunar surface: Low energy ion measurement by MAP-PACE onboard SELENE (KAGUYA), Geophys. Res. Lett., 35, L24205, 2008.

[12] Feuerbacher, B.; Anderegg, M.; Fitton, B.; Laude, L. D.; Willis, R. F.; Grard, R. J. L., "Photoemission from lunar surface fines and the lunar photoelectron sheath", Proceedings of the Lunar Science Conference, vol. 3, p.2655, 1972.

P. Sarrailh, J.-C. Matéo-Vélez and S.L.G. Hess are with the ONERA - The French Aerospace Lab, Toulouse, France (e-mail: Pierre.Sarrailh@onera.fr)

F. Cipriani, D. Rodgers and A. Hilgers are with the ESA/ESTEC, Noordwijk, The Netherlands

B. Jeanty-Ruard, B. Thiébaul and J. Forest are with Artenum, Paris, France

F. Honary and S. Marple are with the University of Lancaster, Departments of Physics, Lancaster, United-Kingdom